Energy Budget Constraints on the Time History of Aerosol Forcing and Climate Sensitivity

C. J. Smith[1,2], G. R. Harris[3], M. D. Palmer[3], N. Bellouin[4], W. Collins[4], G. Myhre[5], M. Schulz[6], J.-C. Golaz[7], M. Ringer[3], T. Storelvmo[8] and P. M. Forster[1]

[1]Priestley International Centre for Climate, University of Leeds, UK.

[2]International Institute for Applied Systems Analysis (IIASA), Laxenburg, Austria.

[3]Met Office Hadley Centre, Exeter, UK.

[4]Department of Meteorology, University of Reading, UK.

[5]Center for International Climate and Environmental Research in Oslo (CICERO), Norway.

[6]Norwegian Meteorological Institute, Oslo, Norway.

[7]Lawrence Livermore National Laboratory, Livermore, CA, USA.

[8]Department of Geosciences, University of Oslo, Norway.

Corresponding author: Chris Smith (c.j.smith1@leeds.ac.uk)

Key Points:

- We determine the most plausible time history of aerosol forcing that matches surface temperature and Earth energy uptake constraints
- Constrained aerosol forcing shows a modest recovery between 1980 and 2014, slower than the rate simulated by many CMIP6 models
- The best estimate aerosol forcing using this method is -1.10 W m^{-2} for 2005-14 relative to 1750.

Abstract

An observationally-constrained time series of historical aerosol effective radiative forcing (ERF) from 1750 to 2019 is developed in this paper. We find that the time history of aerosol ERFs diagnosed in CMIP6 models exhibits considerable variation and explore how the time history of aerosol forcing influences the probability distributions of present-day aerosol forcing and emergent metrics such as climate sensitivity. Using a simple energy balance model, trained on CMIP6 climate models and constrained by observed near-surface warming and ocean heat uptake, we derive estimates for the historical aerosol forcing. We find 2005-2014 mean aerosol ERF to be -1.1 (-1.8 to -0.5) W m^{-2} relative to 1750. Assuming recently published historical emissions from fossil fuel and industrial sectors and biomass burning emissions from SSP2-4.5, aerosol ERF in 2019 is -0.9 (-1.5 to -0.4) W m^{-2}. There is a modest recovery in aerosol forcing (+0.025 W m^{-2} $decade^{-1}$) between 1980 and 2014. This analysis also gives a 5-95% range of equilibrium climate sensitivity (ECS) of 1.8-5.1°C (best estimate 3.1°C) with a transient climate response (TCR) of 1.2-2.6°C (best estimate 1.8°C).

Plain Language Summary

There are two main human drivers of climate change: (i) Greenhouse gas emissions, which warm the planet; and (ii) air pollution (aerosols) that offset some of this warming. Unfortunately, disentangling the effects of historical aerosol cooling is difficult based on the available observations. Therefore, we often use climate models to estimate how much aerosols have cooled the Earth since the start of the Industrial Revolution. Over the mid-to-late 20th Century, some climate models simulate less warming compared to 1850 than has been observed. This may be because aerosol cooling in some climate models is too strong. Our approach combines the relationships between aerosol emissions and their cooling effects on temperature from 11 climate models with simpler representations of the underlying physics. This simpler mathematical framework allows us to more fully account for uncertainty in both the aerosol cooling and its effects on surface temperature and ocean heat uptake by running a much larger set of simulations. Our results suggest that the effect of aerosol cooling has only unwound slowly since 1980, and that it is difficult to determine how sensitive the climate is from this method.

1 Introduction

Aerosol effective radiative forcing remains one of the most uncertain components of the present-day climate (Bellouin, Quaas, et al., 2020). Uncertainty in present-day forcing reduces our ability to confidently predict the future climate response to emissions (Forster et al., 2013) and the level of historical greenhouse gas warming masked by the cooling effect of aerosols (Samset et al., 2018). Aerosol forcing is the largest uncertainty governing future committed warming (Matthews & Zickfeld, 2012; Smith et al., 2019) and remaining carbon budgets consistent with Paris Agreement targets (Mengis & Matthews, 2020). In most future socio-economic scenarios, aerosol forcing is projected to become less negative over the 21st century (Gidden et al., 2019; Huppmann et al., 2018; Rogelj et al., 2018), promoting an increase in the rate of warming unless there is a concurrent reduction in greenhouse gas emissions (Shindell & Smith, 2019). The time history of aerosol ERF is a necessary input to many reduced-complexity climate models (Nicholls et al., 2020), which in turn may be driven by simple emissions-to-forcing based relationships; these simple models find enormous utility when coupled to integrated assessment models (Huppmann et al., 2018).

Given its large uncertainty, aerosol forcing has remained an active research area. Several studies have quantified the aerosol effective radiative forcing (ERF) in the present day relative to pre-industrial based on observations, models, energy balance arguments, or a combination of approaches (Andrews & Forster, 2020; Bellouin, Quaas, et al., 2020; Boucher et al., 2013; Fiedler et al., 2019; Forest, 2018; Forest et al., 2002, 2006; Myhre, Shindell, et al., 2013; Skeie et al., 2018; Smith et al., 2020; Zelinka et al., 2014). Fewer studies have attempted to diagnose a time series of historical aerosol forcing. Murphy et al. (2009) used observations of ocean heat uptake, surface temperature and radiative forcing of long-lived greenhouse gases and volcanic eruptions since 1950 to determine the residual forcing, which was mostly attributed to aerosols. Skeie et al. (2011) and Lund et al. (2018) used chemistry-transport models with prescribed meteorology, evaluated at frequent time slice years since pre-industrial, to determine historical aerosol forcing since 1750. Shindell et al. (2013) used timeslices from 1850, 1930, 1980 and 2000 in full-complexity climate models to estimate the historical aerosol forcing. The most complete historical aerosol forcing time series, for 1750 to 2011, is given in Annex II (Prather et al., 2013) of the Intergovernmental Panel on Climate Change Working Group 1 Fifth Assessment Report (AR5), which takes in multiple lines of evidence including the Skeie et al. (2011) and Shindell et al. (2013) modelling studies.

Our goal is define an aerosol ERF time series from 1750 to 2019 that is consistent with energy balance constraints from observations; effectively to provide an update to AR5 Annex II that takes into account more recent evidence. Here we take a combination of the climate modelling and energy balance approaches. Under the Radiative Forcing (RFMIP) and Aerosol Chemistry (AerChemMIP) Model Intercomparison Projects, historically time-varying aerosol forcing can be diagnosed directly from CMIP6 models. However, in the multi-model mean, CMIP6 model simulations of global-mean surface air temperature (GSAT) are cooler than observations throughout the latter part of the 20th Century before recovering to near-present levels of warming today (Flynn & Mauritsen, 2020). One hypothesis is that aerosol forcing in the 20th Century may be too strong in some CMIP6 models, coupled with high transient climate response (TCR) that causes implausibly rapid recent warming in many models (Tokarska et al., 2020). Nevertheless, CMIP6 models remain an important line of evidence in determining historical aerosol forcing. Unlike for greenhouse gases, proxy records for aerosol forcing are sparse before widespread surface radiation measurements became available in the 1950s (Bellouin, Quaas, et al., 2020; Moseid et al., 2020). No global observations of aerosols were available until the satellite era (late 1970s), whereas CMIP6 models provide aerosol forcing estimates from 1850. Therefore, we use CMIP6 model forcing over the industrial era to inform our estimates of historical aerosol ERF, and "correct" for these responses by constraining the forcing estimates to observations of GSAT and Earth energy uptake (EEU).

2 Methods and Data

This section describes how the historical ERF time series are generated and how observational constraints are used with a simple energy-balance climate model to produce a best estimate and range of historical aerosol forcing estimates. A number of historical aerosol forcing time series are investigated. The primary focus of this study is an ensemble of time series generated from a simple relationship of global annual emissions to global annual historical aerosol ERF, using historical aerosol emissions time series and tuning this relationship (which we call a "forcing emulator") on CMIP6 models where historical aerosol forcing estimates exist. Following the observational constraining we refer to this time series as "CMIP6-constrained".

We also investigate replacing the CMIP6 emissions time series with scaled estimates of historical aerosol forcing from 11 CMIP6 models and one chemistry-transport model. This provides a total of 13 different historical aerosol forcing scenarios.

Throughout this paper, a probabilistic approach is taken, sampling 100,000 historical forcing timeseries per scenario with the same number of simple climate model configurations. Uncertainties in the non-aerosol components of historical forcing (greenhouse gases, land-use change, black carbon deposition on snow, aviation contrail and contrail cirrus, and natural forcings) are also taken into account. The resulting GSAT and EEU time series from each ensemble member is compared to the observational constraints and a weighted posterior distribution produced of historical aerosol ERF.

2.1 Aerosol effective radiative forcing timeseries

2.1.1 CMIP6 model output

We start with 1850 to 2014 (or beyond) transient aerosol ERF derived from 11 GCMs (Fig. 1; Table 1). Seven models were provided under RFMIP (Pincus et al., 2016), three under AerChemMIP (Collins et al., 2017) and one used a similar method to AerChemMIP but with Atmospheric Model Intercomparison Project (AMIP) sea-surface temperatures (SSTs) rather than model-diagnosed SSTs (Golaz et al., 2019).

Table 1: CMIP6 models providing transient historical aerosol ERF estimates. Runs extended beyond 2014 in RFMIP experiments followed an SSP2-4.5 forcing pathway.

Model	Long name	Model variants	Modelling protocol	Ensemble members	Time period	References
CanESM5	Canadian Earth System Model, verison 5.0.3	r1i1p2f1 r2i1p2f1 r3i1p2f1	RFMIP	3	1850-2100	Swart et al. (2019)
E3SM-1-0	U.S. Department of Energy (DOE) Energy Exascale Earth System Model (E3SMv1)	3 ensemble member pairs (non-ESGF)	AMIP and AMIP with pre-industrial aerosols	3	1870-2014	Golaz et al. (2019)
GFDL-ESM4	Geophysical Fluid Dynamics Laboratory ESM4.1	r1i1p1f1	AerChemMIP	1	1850-2014	Dunne et al. (2020)
GFDL-CM4	Geophysical Fluid Dynamics Laboratory CM4.0	r1i1p1f1 r3i1p1f1	RFMIP	2	1850-2100	Held et al. (2019)
GISS-E2-1-G	Goddard Institute for Space Studies ModelE 2.1-G	r1i1p1f2	RFMIP	1	1850-2100	Kelley et al. (2020)
HadGEM3-GC31-LL	Met Office Hadley Centre Global Coupled Model 3.1	r1i1p1f3 r2i1p1f3 r3i1p1f3	RFMIP	3	1850-2099	Williams et al. (2018)
IPSL-CM6A-LR	Institut Pierre Simon Laplace	r1i1p1f1	RFMIP	1	1850-2100	Boucher et al. (2020)

	Climate Model 6A (low resolution)					
MIROC6	Model for Interdisciplinary Research on Climate, version 6	r1i1p1f1 r2i1p1f1 r3i1p1f1	RFMIP	3	1850-2100	Tatebe et al. (2019)
MRI-ESM2-0	Meteorological Research Institute Earth System Model version 2.0	r1i1p1f1	AerChemMIP	1	1850-2014	Yukimoto et al. (2019)
NorESM2-LM	Norwegian Earth System Model, version 2	r1i1p2f1 r2i1p2f1 r3i1p2f1	RFMIP	3	1850-2100	Seland et al. (2020)
UKESM1-0-LL	UK Earth System Model	r1i1p1f4	AerChemMIP	1	1850-2014	Sellar et al. (2019)

In all cases, aerosol ERF is diagnosed as the top-of-atmosphere radiation flux difference between parallel climate model experiments, one with time-varying aerosols, and one with pre-industrial aerosols (Table 2). In the RFMIP models, SSTs, sea ice and non-aerosol forcings are given as a pre-industrial climatology in both the transient (CMIP6 name piClim-histaer) and control (piClim-control) experiments, with aerosols following the 1850 to 2014 (or 2100, in models running the SSP2-4.5 extension) emissions from CMIP6 in the transient run (Hoesly et al., 2018; van Marle et al., 2017). The pre-industrial control is a 30-year climatology. In AerChemMIP models we use historical (1850-2014) SSTs, sea ice and forcings (histSST) as the perturbation experiment, and historical SSTs, sea-ice and non-aerosol forcings with pre-industrial aerosols (histSST-piAer) as the control. E3SM also followed this method (described in Golaz et al. (2019)).

Table 2: Experiment definitions for the RFMIP and AerChemMIP model runs used in this study.

Protocol	**Experiment**	**Control**
RFMIP	CMIP6 name piClim-histaer	CMIP6 name piClim-control
	Pre-industrial SSTs & sea ice	Pre-industrial SSTs and sea ice
	Pre-industrial non-aerosol forcing	Pre-industrial non-aerosol forcing
	Historical aerosol forcing	Pre-industrial aerosol forcing
AerChemMIP	CMIP6 name histSST	CMIP6 name histSST-piAer
	Historical SSTs & sea ice	Historical SSTs & sea ice
	Historical non-aerosol forcing	Historical non-aerosol forcing
	Historical aerosol forcing	Pre-industrial aerosol forcing

Figure 1 shows the aerosol effective radiative forcing with respect to 1850 from CMIP6 models. Most models show a peak in negative aerosol forcing at some point between 1975 and 2010 before recovering in recent years.

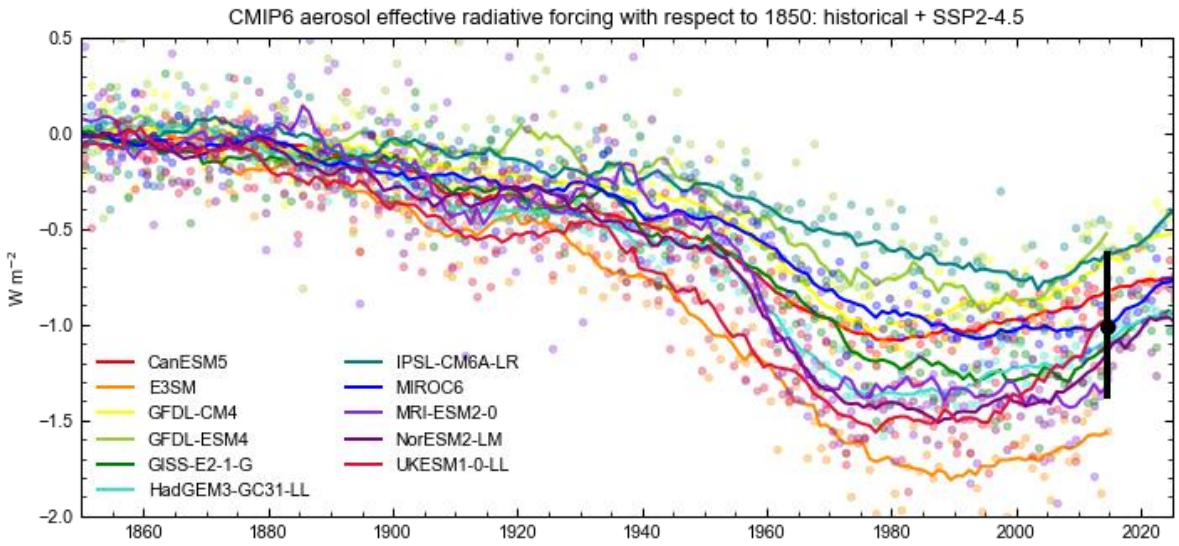

Figure 1: CMIP6 diagnosed net aerosol effective radiative forcing relative to an 1850 climatology. Individual years are shown in dots with an 11-year Savitzky-Golay smoothing filter applied to show solid lines. The black point and line represents the 17-model mean and range from Smith et al. (2020) for 1850-2014, which did not include E3SM-1-0.

2.1.2 Separation of aerosol components

For each CMIP6 model, the shortwave (SW) aerosol-radiation and aerosol-cloud interaction components of the ERF ($ERFari_{SW}$ and $ERFaci_{SW}$) are determined using the Approximate Partial Radiative Perturbation (APRP) method (Taylor et al., 2007; Zelinka et al., 2014). The LW ERF from aerosol-cloud interactions ($ERFaci_{LW}$) was determined using the difference between all-sky and clear-sky forcing (difference in cloud radiative effect) with the LW ERF from aerosol-radiation interactions ($ERFari_{LW}$) estimated as the difference between ERF_{LW} and $ERFaci_{LW}$. The APRP is not exact and a small residual term arises that varies over time and by model (Fig. S1), some of which is related to a small surface albedo adjustment (Ghan, 2013), but only the time-varying shapes and relative magnitudes of ERFari and ERFaci to each other are important for this decomposition.

For the RFMIP models we calculate the APRP using the difference of each year of the piClim-histaer run against every year of the piClim-control run before averaging across the 30 piClim-control years to determine the ERFari and ERFaci from each year of 1850 to 2014 (or 2100). This method removes some non-linearities in the APRP (particularly in relation to the cloud fraction adjustment part of ERFaci) alongside minimising the influence of internal variability. For the AerChemMIP models and E3SM-1-0, APRP was calculated using the parallel all-forcing and 1850-aerosol forcing AMIP ensemble members and averaged. In all cases where modelling groups provided more than one ensemble member, the APRP decomposition is calculated separately in each ensemble member and then averaged.

2.1.3 Forcing emulator

Simple emissions-based relationships are then fit to the APRP-derived ERFari and ERFaci in each CMIP6 model:

$$\mathrm{ERFari} = \alpha_{\mathrm{SO2}} E_{\mathrm{SO2}} + \alpha_{\mathrm{BC}} E_{\mathrm{BC}} + \alpha_{OC} E_{\mathrm{OC}} \quad (1)$$

$$\mathrm{ERFaci} = -\beta \ln(1 + E_{\mathrm{SO2}}/s_{\mathrm{SO2}} + (E_{\mathrm{BC+OC}}/s_{\mathrm{BC+OC}})) \quad (2)$$

In eqs. (1) and (2), E_{SO2}, E_{BC} and E_{OC} refer to global annual total emissions in Tg yr^{-1} of SO_2, black carbon (BC) and organic carbon (OC), and α_{SO2}, α_{BC}, α_{OC}, β, s_{SO2} and $s_{\mathrm{BC+OC}}$ are scaling coefficients. α values can be interpreted as the radiative efficiency of emission of each aerosol species. Strictly, eqs. (1) and (2) represent radiative effects rather than radiative forcings. Radiative forcings are given by the difference of radiative effects in eqs. (1) and (2) calculated between the emissions in the year of interest and the pre-industrial year (either 1850 or 1750).

Equation (1) follows from studies showing that ERFari scales linearly with emissions (Johnson et al., 2019; Lund et al., 2018; Mahajan et al., 2013; Rap et al., 2013). Equation (2) is an extension of the simple relationship of Stevens (2015) and is based on the understanding that the change in cloud albedo is logarithmic with sulfate burden, and that burden scales with emissions (Carslaw et al., 2013; Charlson et al., 1992). Including carbonaceous aerosol in eq. (2) represented by the sum of BC and OC emissions is useful as some CMIP6 models include the effects of BC and/or OC on the change in cloud condensation nuclei. The resulting aerosol-cloud interactions can be substantial, for example a negative ERFaci to BC emissions in the MIROC6 model (Thornhill et al., 2020). Equation (2) is found to give a good heuristic approximation of global-mean ERFaci to a more sophisticated aerosol indirect effect model (Ghan et al., 2013) as shown in Smith, Forster, et al. (2018). The sum of BC and OC emissions is used following the original Ghan et al. (2013) aerosol indirect model which considers primary anthropogenic emissions to be BC+OC, and to limit the number of free parameters in eq. (2) to three.

α_{SO2}, α_{BC}, α_{OC}, β, s_{SO2} and $s_{\mathrm{BC+OC}}$ parameters in eqs. (1) and (2) are estimated using a least-squares curve fit of each CMIP6 model's ERFari and ERFaci (Table 3). A multi-model mean emulation is performed where the ERFari and ERFaci from the 11 models is averaged and eqs. (1) and (2) applied. The multi-model mean α coefficients (-2.5, +28.5 and -8.5 mW m^{-2} (Tg yr^{-1})$^{-1}$ for SO_2, BC and OC respectively) are of similar magnitudes to the radiative efficiencies from Aerocom models (Myhre, Samset, et al., 2013) for SO_2 and BC, and a little stronger for OC here. The radiative efficiency coefficients are negative for BC and positive for OC in the IPSL-CM6A-LR model. However, using coefficients derived from the AerChemMIP single-forcing experiments for BC, OC and SO_2 in IPSL-CM6A-LR-INCA gives a much less good fit to the historical aerosol forcing in IPSL-CM6A-LR than our fitted coefficients, and while the fitted coefficients may not be representative of the true physical behavior in this model, allowing these values as part of the prior sampling allows for a larger diversity of aerosol forcing time series. We do not attribute a nitrate forcing to avoid overfitting and because most models do not include the effects of nitrogen compounds on aerosol formation. In reality, nitrate formation may compete with sulfate formation for available ammonium. Evidence suggests this is of limited importance historically (Thornhill et al., 2020), but may become more important in future scenarios where the nitrate to sulfate emissions ratio is projected to increase (Bellouin et al., 2011; Hauglustaine et al., 2014).

The best-fit values for s_{SO2} and $s_{\mathrm{BC+OC}}$ span several orders of magnitude. We treat these terms as shape parameters, describing how linear or logarithmic the change in ERFaci is with increasing anthropogenic SO_2 and carbonaceous aerosol emissions. With large s_{SO2} and $s_{\mathrm{OC+BC}}$ values, a linear response in ERFaci to emissions is exhibited (from the Taylor expansion of $\ln(1+x) \approx x$ for small x). The degree of logarithmic behaviour that ERFaci exhibits to emissions differs considerably between GCMs (Wilcox et al., 2015) and the possibility that ERFaci may be linear with emissions in some CMIP5 models was discussed in Booth et al. (2018).

Table 3: Forcing emulator coefficients corresponding to eqs. (1) and (2) for each model and the emulation of the multi-model mean forcing. Emissions are in terms of $TgSO_2$ for α_{SO2} and TgC for α_{BC} and α_{OC}.

	ERFari (mW m^{-2} (Tg yr^{-1})$^{-1}$)			**ERFaci**		
Model	α_{SO2}	α_{BC}	α_{OC}	β (W m^{-2})	s_{SO2} (TgSO$_2$ yr^{-1})	s_{BC+OC} (TgC yr^{-1})
CanESM5	-2.5	32.6	-0.4	0.727	58.9	24.6
E3SM-1-0	-0.9	24.8	-12.6	2.048	155.9	71.3
GFDL-CM4	-2.6	26.9	-2.1	3.501	692.7	382.9
GFDL-ESM4	-2.6	102	-30.4	3096	913 500	202 620
GISS-E2-1-G	-6.7	146	-44.1	0.563	117.9	16.0
HadGEM3-GC31-LL	-2.9	10.2	1.5	1.004	95.4	77.2
IPSL-CM6A-LR	-0.7	-56.1	8.8	1.097	358.3	518.9
MIROC6	-1.8	38.7	-14.2	0.773	117.2	35.0
MRI-ESM2-0	-3.2	4.5	-10.0	7.404	1276	907.4
NorESM2-LM	-1.5	-18.3	9.7	13502	1 915 000	944 800
UKESM1-0-LL	-2.4	2.6	0.0	0.741	39.5	228.1
Multi-model mean emulation	-2.5	28.5	-8.5	1.223	156.5	76.7

Figure 2 shows the emulated fits to each CMIP6 model from eqs. (1) and (2) as colored curves with the APRP-derived forcing from the GCMs in grey using an 1850 reference. The gray curves in Figure 2 show that most models show a peak in ERFari that is weakening in recent years, whereas for ERFaci is approximately constant up to 2014 or with a slower weakening trend. It can be seen that the emulated relationships (colored curves) give good representations of each component of the aerosol forcing in each model. We extrapolate these CMIP6 model-specific emulations back to 1750 in each model, resulting in a small positive forcing in 1750 relative to 1850. Where models do not provide an SSP2-4.5 future projection, we also extend these time series forward using eqs. (1) and (2). Finally, we re-base all emulated time series to a 1750 reference (fig. 3), where the impacts of the different shapes for historical aerosol forcing due to different parameter combinations are more clearly seen. One notable feature in all time series is an increased forcing between 2014 and 2015 in the emulated curves owing to a 16% reduction in global SO_2 emissions from the CMIP6 historical to SSP2-4.5 datasets over one year.

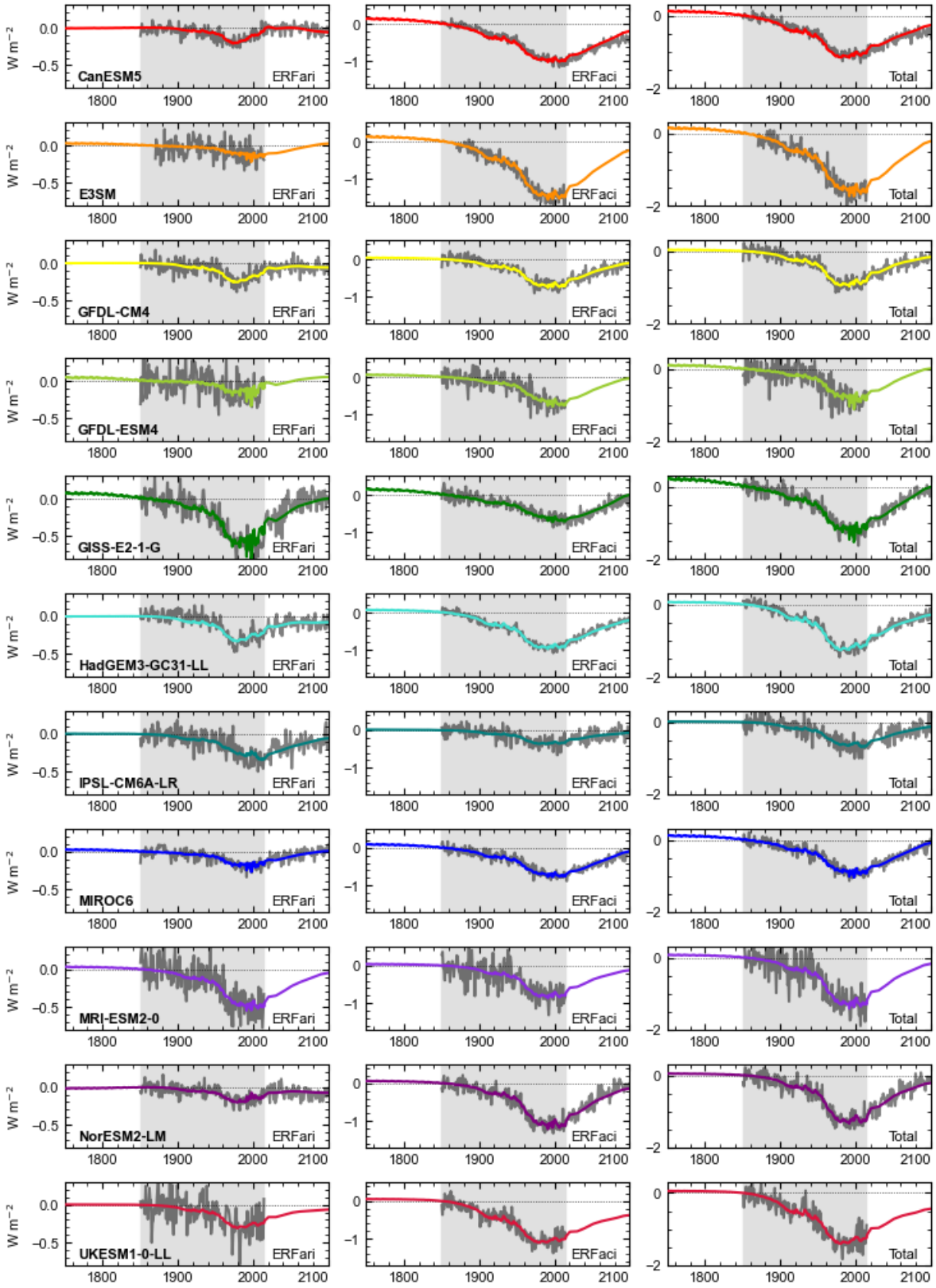
CanESM5
E3SM
GFDL-CM4
GFDL-ESM4
GISS-E2-1-G
HadGEM3-GC31-LL
IPSL-CM6A-LR
MIROC6
MRI-ESM2-0
NorESM2-LM
UKESM1-0-LL
ERFari
ERFaci
Total
W m⁻²
1800
1900
2000
2100

Figure 2: simple emissions-based fits from eqs. (1) and (2) to ERFari (left), ERFaci (centre) and total aerosol forcing (right) for 11 CMIP6 models. Gray curves show the relevant forcing components from each GCM diagnosed using the APRP method.

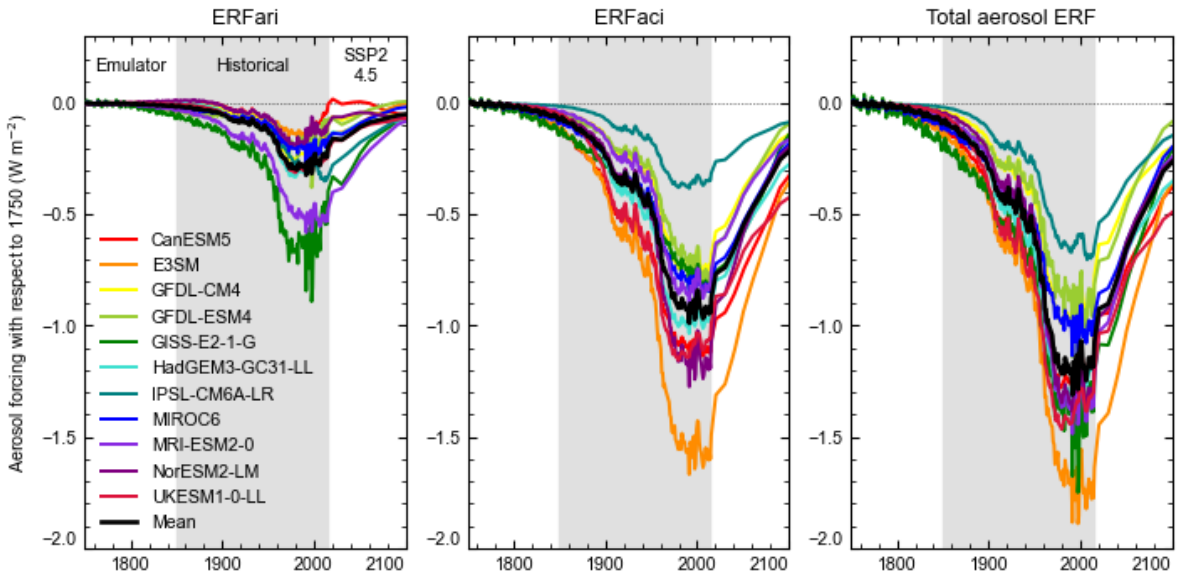

Figure 3: Emulated emissions to forcing curves, relative to 1750. The multi-model mean emulation is shown in black.

2.1.4 Ensemble generation

To simulate time-varying aerosol forcing we take probabilistic ensembles for both the magnitude and the shape of the historical aerosol forcing. To generate historical shapes, we take 100,000 samples of α_{SO2}, α_{BC}, α_{OC}, s_{SO2} and s_{BC+OC} based on their distributions from the 11 participating GCMs (Table 3). A joint kernel-density estimate of the α coefficients is used to derive a distribution which is then sampled from for ERFari (Fig. 4a-c). Accounting for correlation between the coefficients maintains the connection that different aerosol species are often co-emitted. For ERFaci, we take ln (s_{SO2}) and ln (s_{BC+OC}) from each model and derive a joint kernel distribution from these two parameters (Fig. 4d). Logarithms of the values in Table 3 are used because the total ERFaci in Eq. (2) has a logarithmic relationship to emissions and individual model estimates of these parameters span several orders of magnitude. β is not a degree of freedom in this setup because the resultant ERFaci time series will be scaled as described below.

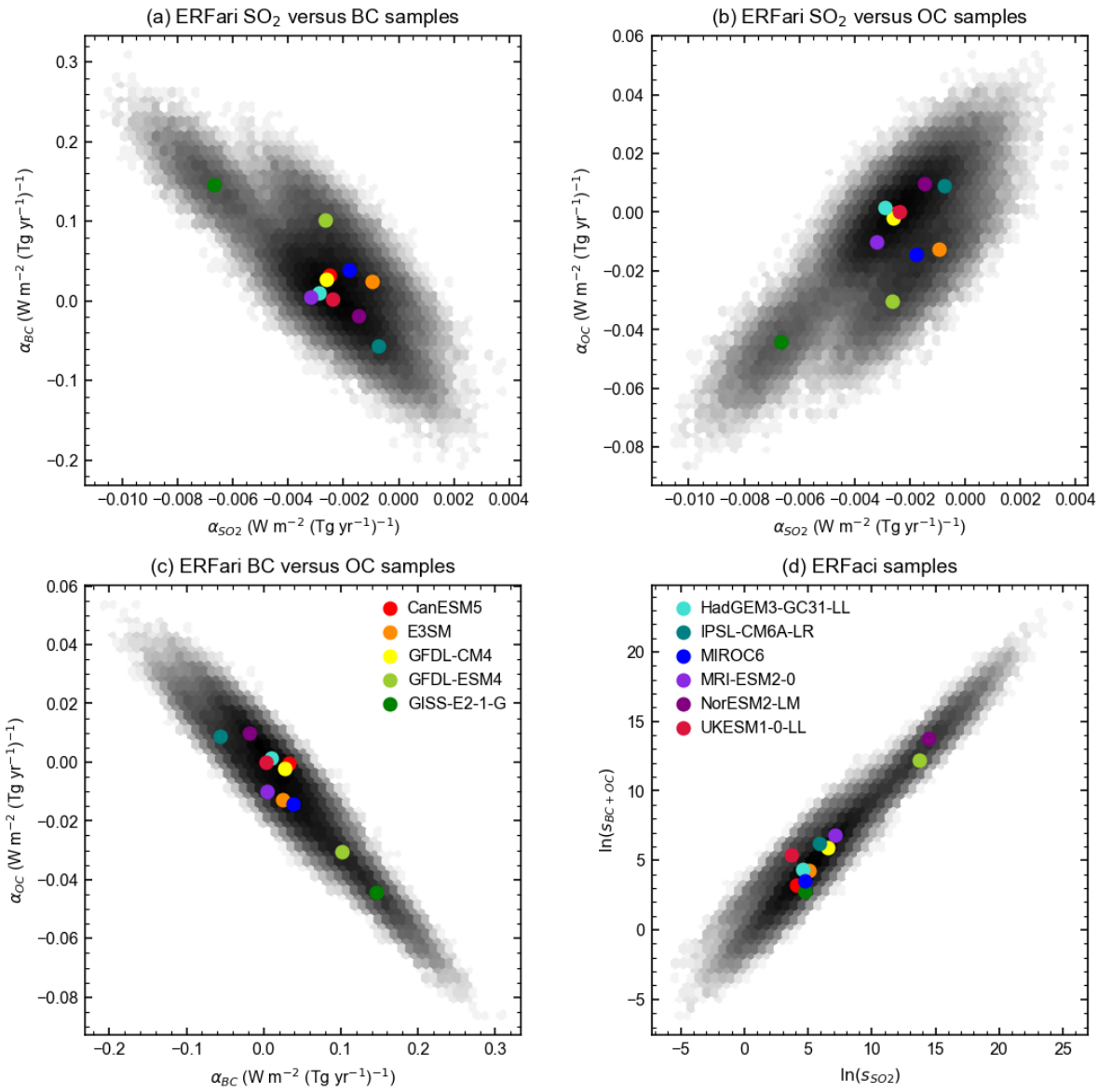

Figure 4: Joint distributions of (a) α_{SO2} and α_{BC}, (b) α_{SO2} and α_{OC}, (c) α_{BC} and α_{OC}, (d) ln (s_{SO2}) and ln (s_{BC+OC}). The grayscale 2D hexbin histogram of points represents a density of the 100,000 drawn sample sets and the coloured points are fits to each CMIP6 model.

We combine the sampled α and s coefficients with 100,000 samples of the absolute values of the 1850 to 2005-15 ERFari and ERFaci from the process-based assessment in fig. 8 of Bellouin, Quaas, et al. (2020; hereafter the "Ringberg assessment"), using the distributions that do not account for energy budget constraints. We run the emissions emulator in eqs. (1) and (2) using a update of the historical CEDS emissions to 2019 (O'Rourke et al., 2020) for energy and industrial sectors and BB4CMIP (for biomass burning) under a historical+SSP2-4.5 assumption (the emissions are much less sensitive to the choice of scenario for biomass burning than for energy and industry). Critically, the updated CEDS emissions account for phenomena such as an earlier and more gradual reduction in SO_2 emissions from China than were in the original CMIP6

dataset (Paulot et al., 2018), as well as other corrections, and avoids arbritrarily choosing a scenario for post-2014 emissions. Differences in these time series are plotted in Fig. S2.

This process rescales the α coefficients and selects β in each ensemble member consistent with the present-day ERFaci. These 100,000 sampled time series are then rebased to a 1750 baseline by subtracting the 1750 forcing from the 1850 forcing, producing 100,000 candidate historical time series of aerosol forcing for the period 1750-2019 that differ in shape and magnitude (Fig. 5).

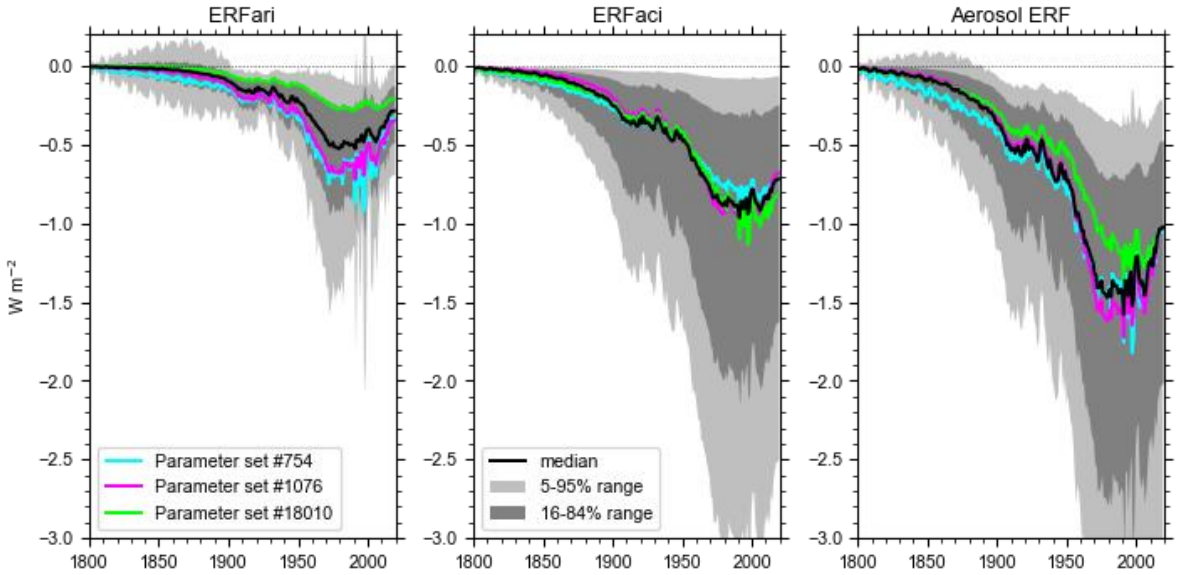

Figure 5: Sampled ERFari, ERFaci and total aerosol ERF time series before constraint. Overplotted are three individual ensemble members (colored lines) that have present-day total aerosol forcing close to the ensemble mean with different time histories. The 5-95% and 16-84% ranges of the ensemble are shown as light and dark grey bands with the ensemble median in black.

2.1.5 Scaled model forcing

Alongside the emissions-based aerosol forcing time series, we repeat the analyses using scaled historical ERFari and ERFaci from each CMIP6 model, where the shapes of the historical forcing derived from the APRP method (Fig. 2) in each model are fixed, but the pre-industrial to present-day magnitudes are allowed to vary. We also use RFari and RFaci time series generated from the Oslo-CTM3 chemistry transport model (Lund et al., 2018, 2019) for 1750-2020 under historical+SSP2-4.5. In these 11 CMIP6 models plus Oslo-CTM3, the magnitude of 1850 to 2005-15 forcing is allowed to vary according to the Ringberg assessment distributions, and the generated time series are extrapolated backwards to a 1750 baseline. Unlike the emissions time series run with the forcing emulator, the historical shapes of ERFari and ERFaci from these 12 model estimates are fixed.

2.2 Non-aerosol forcing time series

The non-aerosol component forcings are also generated from a 100,000-member Monte Carlo ensemble. As they are either less uncertain or smaller in magnitude (or both) than the aerosol forcing they are not the main focus of this paper but are generated to provide a consistent view of the total ERF, including uncertainty estimates, so that energy budget constraints can be applied. Detailed information is provided in Supplementary Text S1 with a summary of the key data sources in Table 4.

Table 4: Non-aerosol forcing present-day uncertainties and key references.

Forcing type	Description	Key references
Well-mixed greenhouse gases	Concentrations to radiative forcing; tropospheric adjustments	Etminan et al. (2016); Gidden et al. (2019); Hodnebrog, Aamaas, et al. (2020); Hodnebrog, Myhre, et al. (2020); Meinshausen et al. (2017, 2020); Smith et al. (2020); Smith, Kramer, et al. (2018)
Ozone	Analysis of CMIP6 models; precursor emissions to forcing	Skeie et al. (2020); Smith, Forster, et al. (2018); Stevenson et al. (2013)
Other anthropogenic	Land use forcing (including irrigation); black carbon on snow; aviation contrails; stratospheric water vapor from methane oxidation	Bond et al. (2013); Ghimire et al. (2014); Lee et al. (2020); Myhre, Shindell, et al. (2013); Sherwood et al. (2018)
Volcanic	Forcing from stratospheric aerosol optical depth	Global Volcanism Program (2013); Gregory et al. (2016); Kovilakam et al. (2020); Larson & Portmann (2016); Toohey & Sigl (2017)
Solar	Total solar irradiance; tropospheric adjustments	Gray et al. (2009); Matthes et al. (2017); Smith, Kramer, et al. (2018); Vieira et al., (2011)

2.3 Simple climate model

We use our 100,000 member ensemble of aerosol and non-aerosol forcings and run them in a two-layer energy balance model, including efficacy of deep-ocean heat uptake (Geoffroy, Saint-Martin, Bellon, et al., 2013; Geoffroy, Saint-Martin, Olivié, et al., 2013; Held et al., 2010). To perform this many simulations precludes the use of a comprehensive GCM and similar constrained Monte Carlo ensemble methods using reduced-complexity models have been done previously (Meinshausen et al., 2009; Smith, Forster, et al., 2018). The structural uncertainty associated with the choice of simple climate model has been found to have limited impact on global mean temperature projections in historical simulations (Nicholls et al., 2020). We choose to use the two-layer model due to its computational efficiency, inclusion of both EEU and GSAT, and its proven ability as a useful emulator of complex GCMs (Palmer et al., 2018). We use the formulation from the two Geoffroy et al. papers, hereafter G13a and G13b. The two-layer model can be written as

$$C_{\mathrm{mix}} \frac{dT_{\mathrm{mix}}}{dt} = F + \lambda T_{\mathrm{mix}} - \epsilon\gamma(T_{\mathrm{mix}} - T_{\mathrm{deep}}) \quad (3)$$

$$\epsilon C_{\mathrm{deep}} \frac{dT_{\mathrm{deep}}}{dt} = \epsilon\gamma(T_{\mathrm{mix}} - T_{\mathrm{deep}}) \quad (4)$$

where C_{mix} and C_{deep} (W yr m^{-2} K^{-1}) are the heat capacities of the ocean mixed layer and deep ocean, T_{mix} and T_{deep} (K) are the respective layer temperature anomalies, λ (W m^{-2} K^{-1}) is the climate feedback parameter (using the convention that negative values indicate stabilizing feedbacks), F (W m^{-2}) is the effective radiative forcing, ε (dimensionless) is the efficacy of deep ocean heat uptake and γ (W m^{-2} K^{-1}) the heat transport between the two layers. The relatively small heat capacity of the land surface and atmosphere compared to the ocean means that it can be neglected and the GSAT anomaly is given by T_{mix}.

All available 44 CMIP6 models that published both abrupt-4xCO2 and piControl simulations to the Earth System Grid Federation as of 2 July 2020 were used to tune the two-layer model using the method set out in G13a and G13b. Models that were available on different resolutions (e.g. NorESM2-LM and NorESM2-MM), and physical and Earth system models from the same group (e.g. CNRM-CM6-1 and CNRM-ESM2-1) were treated as separate models, but different physics versions of the same model were not (e.g. r1i1p1f1 and r1i1p3f1 from GISS-E2-1-G). The two-layer model is tuned to the GSAT and TOA radiation imbalance of each CMIP6 model's abrupt-4xCO2 run. There are five free parameters in the G13b model: γ, ε, λ, C_{mix} and C_{deep}. Radiative forcing from a quadrupling of CO_2 ($F_{4\times}$) is also calibrated using this method with the abrupt-4xCO2 experiments. Table S1 sets out the parameters for each model and Fig. S3 shows the temperature evolution in CMIP6 models for the model output and the simulated two-layer model fits for abrupt-4xCO2. The ECS is an emergent parameter from this model and is calculated as $F_{4\times}/-2\lambda$. The inclusion of the efficacy of ocean heat uptake in the two-layer model leads to different and often larger estimates of climate sensitivity than from a "Gregory regression" of TOA energy imbalance against global mean temperature anomaly for the first 150 years of abrupt-4xCO2 (the so-called "effective" climate sensitivity, EffCS). The strengthening of climate feedbacks over time as temperatures approach equilibrium in abrupt-4xCO2 experiments results in the long-term equilibrium ECS being in the region of 10-30% larger than EffCS (Rugenstein et al., 2020). The version of the two-layer model that includes efficacy of ocean heat uptake captures this effect somewhat, and we cautiously refer to our derived climate sensitivity as ECS for this reason.

A joint kernel density estimate distribution of the six input parameters to the two-layer model are sampled based on the values resulting from the 44 CMIP6 model tunings (marginal distributions for each parameter are shown in Fig. S4). The joint distribution allows for correlation between model parameters to be taken into account when sampling (Table S2).

Internal variability in GSAT is simulated by analysing the piControl run in all available models (49 as of 2 July 2020). Global mean temperatures from the piControl simulations are detrended to remove any residual drift with the residuals around the long term trend taken to be the internal variability. The autocovariance matrix of these residuals in each model is constructed by regressing the time series with itself at lag 1 year, lag 2 years, …, lag *n* years where *n* is the length of the model's piControl simulation. This input is then used as the covariance of a multivariate Gaussian distribution that governs the time-dependent internal variability of temperatures in each model. For each ensemble member simulated, one of the 49 CMIP6 models is selected at random, and 270 years (1750-2019) of internal variability generated based on the underlying distribution in the selected GCM. This allows for a more realistic construction of internal variability than a memoryless process noting that in reality events such as ENSO tend to

cluster warm and cool years, and also provides for the recreation of low-frequency long-term internal variability that is present in some models such as CNRM-ESM2-1 (Fig. S5).

2.4 Observational constraints

We use GSAT estimates from 1850-2019 and total Earth system energy uptake observations from 1971-2018 to constrain our simulations. To estimate GSAT we use the Cowtan & Way (2014) dataset of infilled global-mean surface temperatures (GMST; near-surface temperatures over land and sea-ice and sea-surface temperatures over open ocean) for 1850-2019, multiplied by a time-varying ratio of GSAT/GMST from CMIP5 models under the historical and RCP8.5 pathways from 1861 to 2014 (Richardson et al., 2016). This ratio converges towards 1.08 for the recent past (Rogelj et al., 2019) and we extend this ratio forward to 2019. Both observations and model output are rebased to the 1850-1900 mean as a proxy for pre-industrial following the IPCC Special Report on 1.5°C. This results in a central estimate of GSAT warming of 1.10°C for 2010-19 relative to 1850-1900 with a warming trend of 0.30°C per decade since 2010.

For observations of total Earth energy uptake, we use data from the Global Climate Observing System (GCOS) observational dataset that includes estimates from ocean heat uptake, cryosphere, atmosphere and land surface (Von Schuckmann et al., 2020). The ocean has absorbed 89% of the total energy uptake in the Earth system since 1960 owing to its larger thermal capacity compared to other components of the Earth system. The two-layer model only tracks heat uptake into the ocean, but to be physically consistent with the total observed EEU we assume that the heat uptake of the atmosphere, cryosphere and land is taken into account in the heat uptake of the mixed layer of the ocean. The GCOS dataset extends back to 1960, but we focus on the period from 1971-2018 due to the limited coverage of deep ocean temperature observations before the advent of expendable bathythermographs (XBTs) in the late 1960s (Palmer, 2017). Our constraint is based on the agreement of EEU calculated in the two-layer model with the total EEU from 1971 to 2018 in GCOS of 358 ± 37 ZJ (1 s.d.).

Following the running of the two-layer model, each of the 100,000 ensemble members is assigned a weight w_i based on how well it reproduces GSAT and EEU observations. The weighting is based on the model weighting technique of Knutti et al. (2017):

$$w_i = \exp\left(-\left(\frac{r_{\mathrm{GSAT},i}{}^2}{\sigma_{\mathrm{GSAT,D}}{}^2} + \frac{r_{\mathrm{EEU},i}{}^2}{\sigma_{\mathrm{EEU,D}}{}^2}\right)\right) \quad (5)$$

where $r_{X,i}$ is a measure of how well the model reproduces observations for variable X for ensemble member i, and $\sigma_{X,\mathrm{D}}$ is the "radius of model quality" (Sanderson et al., 2015). The radius of model quality is a subjective choice and for both GSAT and EEU we use assessed uncertainties. For GSAT, $r_{\mathrm{GSAT},i}$ represents the root-mean-square error (RMSE) of each ensemble member's simulated temperature compared to observations and $\sigma_{\mathrm{GSAT,D}}$= 0.12°C based on the "likely" (> 66%) range of GMST from the 1850-1900 period to 2006-15 in IPCC Special Report on Global Warming of 1.5°C. For EEU, we use $r_{\mathrm{EEU},i}$ as the difference in EEU between the model ensemble member and the GCOS best estimate of 358 ZJ (1971-2018) and use the

GCOS uncertainty of $\sigma_{EEU,D}$= 37 ZJ. Unlike in Knutti et al. (2017) we do not downweight similar ensemble members.

Following calculation of each w_i, the ensemble weights are normalised such that $\sum w_i = 1$. Although subjective, our choices for the goodness-of-fit to the constraints ensure that GSAT and EEU have approximately equal influence on the total weighting given to each ensemble member (Fig. S6). An ensemble member will receive a high weight if it is close to both observed GSAT and observed EEU resulting in fewer high-weight ensemble members than using a single constraint only. Results using just one constraint are reported in the supplementary material.

3 Results

Figure 6 shows the aerosol ERF time series that best fit the observational constraints of GSAT and EEU for the CMIP6-constrained ensemble plus 12 climate models. Also shown are the projections of GSAT and EEU with the applied ensemble weighting. The weighted 5 to 95% range from the CMIP6-constrained time series using both GSAT and EEU as constraints is shown as a grey band with the weighted mean as a grey line. The 1750-2019 aerosol ERF is determined to be -0.90 W m^{-2} (-1.55 to -0.35 W m^{-2} 5-95% range), comprised from -0.31 (-0.62 to -0.08) W m^{-2} for ERFari and -0.59 (-1.18 to -0.10) W m^{-2} for ERFaci. The central estimate of total aerosol forcing is equal to the -0.9 (-1.9 to -0.1) W m^{-2} assessed for 1750-2011 in AR5, with a narrower "very likely" (> 90%) range in this study.

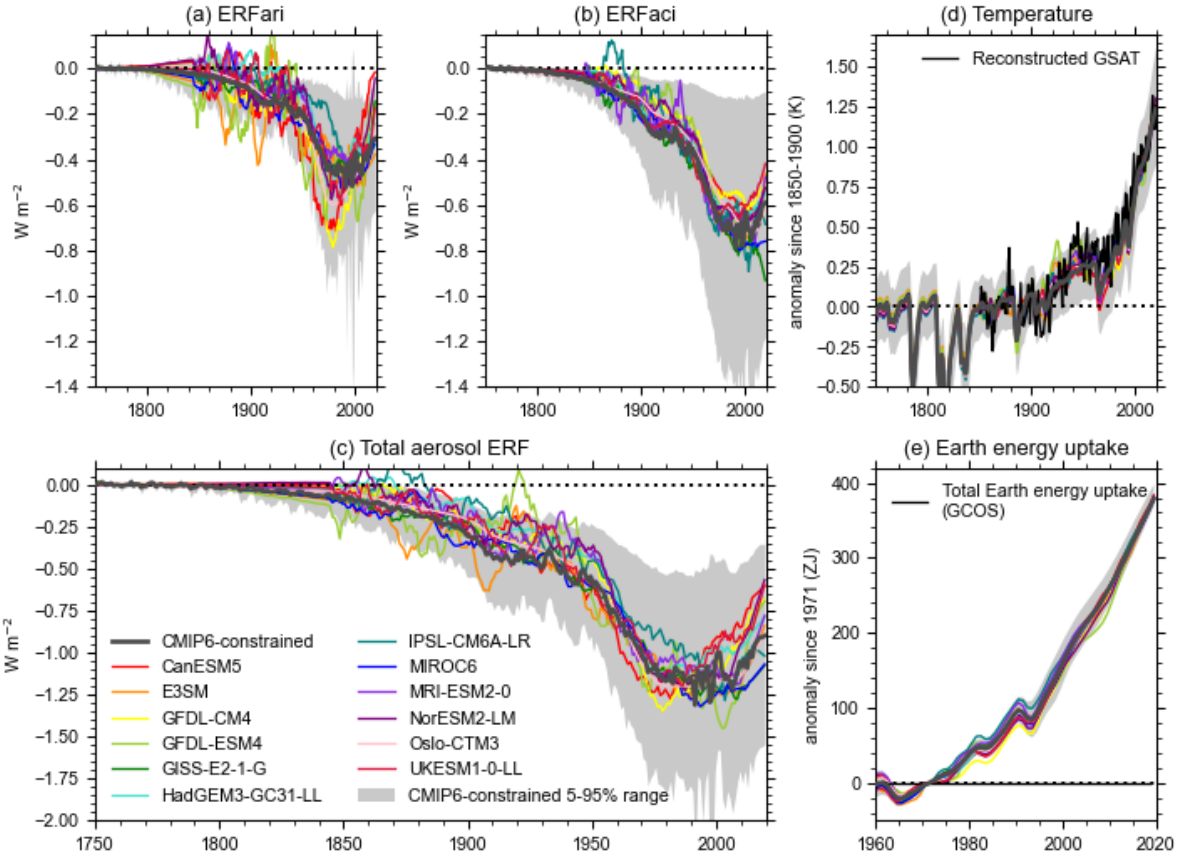

Figure 6: Weighted historical time series of (a) ERFari, (b) ERFaci and (c) total aerosol ERF time history shapes from each forcing scenario. Curves derived from CMIP6 models and Oslo-CTM3 are scaled and ensemble-weighted as described in section 2 and do not represent raw model output. (d) and (e) shows the weighted ensemble simulated global mean surface temperature and ocean heat uptake. Solid lines are weighted ensemble means and shaded regions show the weighted 5th-95th percentiles for the CMIP6-constrained time series.

With the CMIP6-constrained time series, aerosol ERF exhibits a slight recovery between 1980 and 2014 of +0.025 W m^{-2} $decade^{-1}$. This is a lower aerosol recovery than seven of the 11 CMIP6 models, although the constrained 5-95% range is wide (-0.074 to +0.111 W m^{-2} $decade^{-1}$) and includes the means from all but the UKESM1-0-LL model (Fig. 7). These results indicate that a rapid aerosol forcing recovery is unlikely and not consistent with the enegy budget constraints, but whether aerosol forcing has been strengthening, weaking or stable in recent decades is not conclusive.

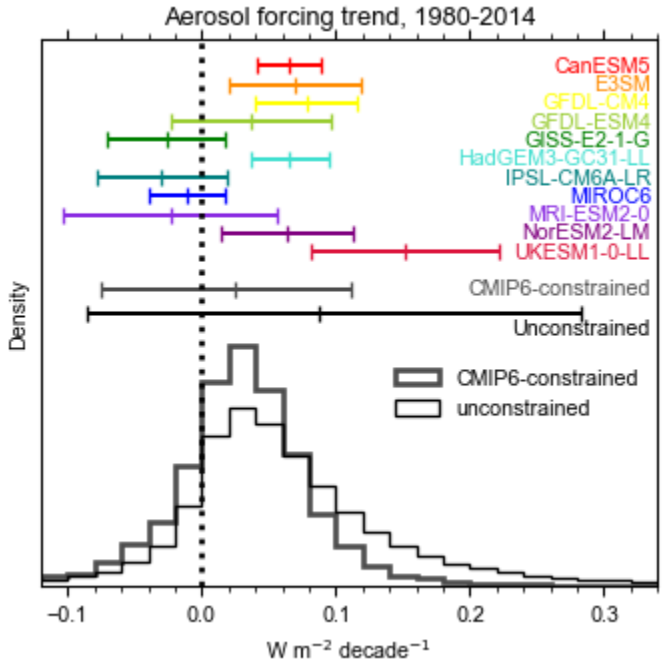

Figure 7: Histograms of linear aerosol forcing trends for 1980-2014 simulated by the 100,000 member Monte Carlo ensemble (thin black histogram) and weighted after application of observational constraints in the CMIP6-constrained time series (thick grey histogram). The mean of these distributions are shown as grey and black lines above the histograms with 5th and 95th percentiles of the constrained and unconstrained distributions. The trends of each CMIP6 model's aerosol forcing are shown as colored lines, calculated as a 35 year regression from 1980-2014 and error bars showing 5-95% confidence ranges in the slope of the regression. Numbers provided in Table S3.

Figure 8 uses the GSAT and EEU constraints to show the present-day distributions of aerosol forcing. Alongside this we use the ensemble weights to calculate distributions of ECS

and TCR from the ensemble given the two-layer model parameter distributions and ensemble weights. To calculate TCR we take the approach of Jiménez-de-la-Cuesta & Mauritsen (2019) noting the TCR is approximately $F_{4\times}/2(-\lambda + \epsilon\gamma)$. The mean, 68% and 90% range for these parameters along with their unconstrained (prior) distributions are shown in Table 5. All 13 historical time series are shown in Table S4 for both GSAT and EEU constraints, and in Tables S5 and S6 using only GSAT or EEU respectively.

A diversity of constrained present-day aerosol ERF distribution shapes is possible for the aerosol forcing from each model's historical time evolution. In particular there are a group of models (the two from GFDL, HadGEM3-GC31-LL, GISS-E2-1-G and NorESM2-LM) where present-day ERFari is relatively weak and few values less than -0.5 W m^{-2} satisfy the observational constraints. For ERFaci, neither the CMIP6 models nor the CMIP6-constrained time series support a strong negative forcing and the constrained distributions are less skewed than the Ringberg assessment range. All historical aerosol forcing time series constrain the present-day aerosol forcing to a narrower range than the full process-based distributions of the Ringberg assessment. As discussed in Bellouin, Quaas, et al. (2020), energy budget constraints do not favour a present-day aerosol forcing more negative than -2 W m^{-2}, and this is also borne out by our distributions in Fig. 8c.

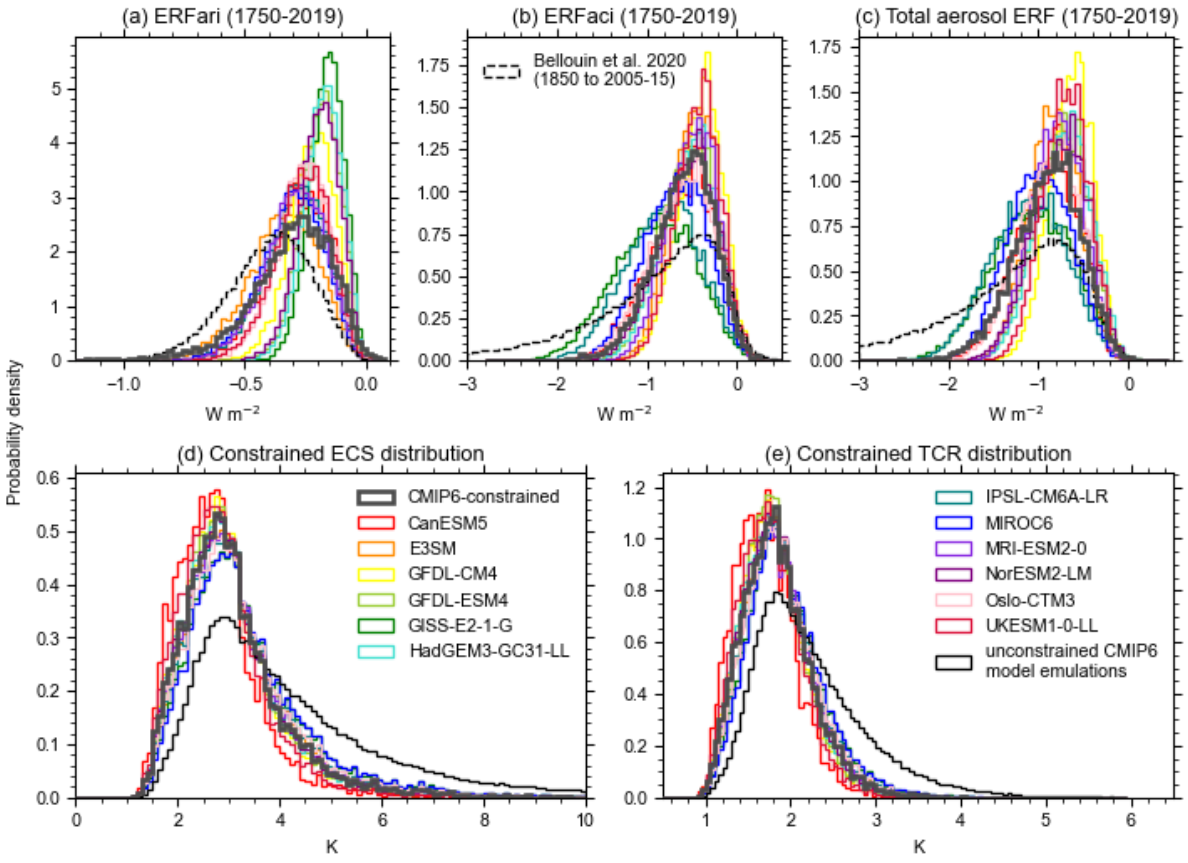

Figure 8: Distributions of (a) ERFari, (b) ERFaci, (c) total aerosol ERF, (d) ECS and (e) TCR. Thin black curves show the prior distributions for aerosol forcing, ECS and TCR.

High values of ECS and TCR are also constrained out when applying observational constraints (Fig. 8d,e). The prior distributions in thin black curves allow for ECS values much larger than those seen in CMIP6 models as values of net feedback λ sampled in the prior distribution (Fig. S4) can be close to zero. Interestingly, the choice of historical aerosol forcing time series is less important for constraining ECS and TCR than for the present-day aerosol forcing, and in every case the constrained distribution favours lower climate sensitivity than the energy-balance derived prior. The constrained distribution of ECS is not tight (1.8 to 5.1°C 5-95% range with a best estimate of 3.1°C), which is lower than the raw CMIP6 model range inferred from the two-layer model fits (1.9 to 7.1°C; Table S1). The best estimates reported in the main body of the text, Table 4 and Figs. 6 and 7 relate to the weighted mean of the constrained distributions; the median estimates are provided in Supplementary Tables 4-6. Transient climate response falls in the 5-95% range of 1.2 to 2.6°C (best estimate 1.8°C).

Table 5: Ensemble percentiles for aerosol forcing, ECS and TCR, for the CMIP6-informed constrained distributions. End dates of 2010 represent a 2005-14 mean.

	Time period	**5%**	**16%**	**mean**	**84%**	**95%**
Total Aerosol ERF (W m^{-2})	**1750-2019**	-1.56	-1.26	-0.90	-0.54	-0.35
	1750-2010	-1.78	-1.50	-1.10	-0.70	-0.48
ERFari (W m^{-2})	**1750-2019**	-0.62	-0.47	-0.31	-0.15	-0.08
	1750-2010	-0.77	-0.59	-0.40	-0.21	-0.12
ERFaci (W m^{-2})	**1750-2019**	-1.18	-0.93	-0.59	-0.26	-0.10
	1750-2010	-1.36	-1.08	-0.69	-0.31	-0.12
ECS (°C)	**Constrained**	1.76	2.15	3.10	3.94	5.11
TCR (°C)	**Constrained**	1.24	1.43	1.83	2.22	2.57

4 Discussion and conclusions

Comprehensive climate models are the best tools available for determining global aerosol forcing where other spatially-complete lines of evidence do not exist, such as prior to the satellite era (approximately 1980). However, model-derived aerosol forcing depends on a chain of processes, and ultimately on spatially-resolved aerosol emissions time series that are themselves uncertain (Hoesly et al., 2018). It is not possible to determine here whether the tendency for some models to project strong aerosol forcing in the second half of the 20th Century and/or too much of a recent aerosol recovery, at least compared to what would be implied by the observational constraints, is due to model processes or uncertainties in the emissions.

It is likely that regional effects are significant and aerosols emitted from different source regions affect the global energy balance in different ways which is not captured in a global emissions to forcing relationship (Kretzschmar et al., 2017). Including how global forcing changes to regional aerosol emissions could be an improvement to the forcing emulator, although may be difficult to implement for aerosol-cloud interactions in marine stratocumulus cloud decks which may be thousands of kilometres from the emissions source (Regayre et al., 2014). However, we show for the 11 GCMs that our relationship is trained on, the forcing emulator works well (Fig. 2) and is useful as a first-order global relationship that incorporates sufficient flexibility in its forcing response to emissions.

Our results are consistent with the conclusions of previous studies that have attempted to constrain present-day aerosol forcing based on energy balance arguments. We find that very large negative values of pre-industrial to present-day aerosol ERF are inconsistent with observed warming and total Earth system energy gain (Andrews & Forster, 2020; Forest, 2018; Forest et al., 2002, 2006; Skeie et al., 2018; Smith, Forster, et al., 2018). Our best estimate 1750-2019 aerosol forcing of -0.90 W m^{-2} is similar to recent observationally-constrained studies that put aerosol forcing in the -0.8 to -0.9 W m^{-2} range (Andrews & Forster, 2020; Skeie et al., 2018; Smith, Forster, et al., 2018), and the review of 19 inverse estimates in Forest (2018) of -0.77 W m^{-2}. We also find that the most likely shape of recent (1980-2014) aerosol forcing is approximately constant or with a slightly positive trend, which is in line with reanalysis-derived estimates of aerosol RFari and RFaci (Bellouin, Davies, et al., 2020), and a rapid recovery in aerosol forcing is not likely.

The shape of historical aerosol forcing time series - whether from our simple emulator or provided by a particular CMIP6 model - does not provide a constraint on the overall 1750-2019 aerosol forcing. However, the choice of aerosol forcing dataset used matters less for constraining ECS and TCR than it does for the shape or magnitude of present-day forcing (Fig. 8). It is difficult to constrain the upper bound of ECS due to the heavy tail of the prior distribution, and 95th percentile values of ECS range from 4.3 to 6.0°C depending on the aerosol forcing time series used (Table S4). Other studies also show that these constrained climate sensitivity distributions are sensitive to the priors used (Sherwood et al., 2020). For example, our prior sample space informed by CMIP6 models has very few ensemble members with ECS < 1.5°C and TCR < 1.0°C, both lower bounds of the respective "likely" range in AR5, and it is possible that this area of the distribution is undersampled. Note that we do not perform a full Bayesian analysis in this paper. However, our ECS estimate of 3.1°C (1.8 to 5.1°C) is in line with, although with wider uncertainty, than the Bayesian estimate of 3.2 (2.3 to 4.7°C) in Sherwood et al. (2020), which takes into account several lines of evidence in their assessment.

The two-layer model used in this study includes the efficacy of deep ocean heat uptake, which can account for the "pattern effect" (Andrews et al., 2018; Sherwood et al., 2020) in which evolving patterns of sea surface temperature change can influence estimates of climate feedback as warming approaches equilibrium. In the notation of Sherwood et al. (2020) the total effective climate feedback can be written $\lambda - \Delta\lambda$ with $\Delta\lambda$ the contribution from the pattern effect. Across the sample of CMIP6 two-layer model calibrations in this study, the pattern effect $\Delta\lambda$ varies from -0.1 to +0.6 W m^{-2} K^{-1} (mean +0.2 W m^{-2} K^{-1}) between 1980 and 2050 (assuming SSP2-4.5 forcing), similar to previous studies (e.g. Armour (2017)). This pattern effect means that historically, the effective climate feedback tends to be slightly weaker than the equilibrium feedback, λ. However, this historical pattern effect is not as large as that determined from observed sea-surface temperatures from AMIP models (Andrews et al., 2018). If we used this approach it is likely our derived historical aerosol forcing would be weaker. However, applying this historical pattern effect approach to our projections is not straightforward. $\Delta\lambda$ requires a 30-year moving window regression to calculate $\Delta\lambda$, and historical simulations in CMIP6 are provided only to 2014 meaning $\Delta\lambda$ can only be estimated until around 2000. $\Delta\lambda$ is sensitive to volcanic eruptions and aerosol forcing (Gregory et al., 2020), and the historical SST record is only one realisation. We therefore do not take the historical approach, but account for the pattern

effect through the samping of deep ocean heat uptake efficacy, and for internal variability through the temporal autocorrelation of piControl runs.

Our results suggest that the limited number of CMIP6 models considered here have a stronger aerosol forcing than may have actually occurred during the 20th Century and this effect may be responsible for the modest warming in the CMIP6 ensemble mean over this time period (0.24 ± 0.22°C for 1961-90 relative to 1850-1900 in CMIP6 models compared to reconstructed GSAT observations of 0.39 ± 0.06°C over the same period; Fig. S7). The diagnosis of historical aerosol forcing in more CMIP6 models to confirm or disprove this would be welcomed. Inclusion of uncertainties in historical emissions would be useful to determine whether this is a factor in suppression of warming. Re-running of GCMs with updated emissions inventories could determine how sensitive models are to emissions uncertainties, and the importance of regional effects. The time history of aerosol forcing and its present-day magnitude both constrain key climate system uncertainties such as climate sensitivity and the rate of recent warming (Tanaka & Raddatz, 2011). Reducing uncertainty in both will reduce uncertainty in climate projections.

Acknowledgments and Data

We thank Tim Andrews and Adriana Sima for provision of prototype versions of the HadGEM3-GC3.1-LL and IPSL-CM6A-LR model outputs respectively, and Maria Rugenstein and Dirk Olivié for helpful discussions. We acknowledge the World Climate Research Programme, which, through its Working Group on Coupled Modelling, coordinated and promoted CMIP6. We thank the climate modeling groups for producing and making available their model output, the Earth System Grid Federation (ESGF) for archiving the data and providing access, and the multiple funding agencies who support CMIP6 and ESGF. C.J.S. was supported by a NERC/IIASA Collaborative Research Fellowship (NE/T009381/1). P.M.F. and C.J.S were supported by European Union's Horizon 2020 Research and Innovation Programme under grant agreement nos. 820829 (CONSTRAIN) and UKRI NERC grant NE/N006038/1 (SMURPHS). G.H. and M.R. were supported by the Joint UK BEIS/Defra Met Office Hadley Centre Climate Programme (GA01101). The Energy Exascale Earth System Model (E3SM) is funded by the U.S. Department of Energy, Office of Science, Office of Biological and Environmental Research. Work at LLNL was performed under the auspices of the U.S. Department of Energy by Lawrence Livermore National Laboratory under contract DE-AC52-07NA27344.

The two layer climate model will be made available on a GitHub repository and the APRP code is available from https://github.com/chrisroadmap/climateforcing/. All code used in the paper will be available at Zenodo and a DOI produced. Cowtan & Way temperature observations are available at https://www-users.york.ac.uk/~kdc3/papers/coverage2013/had4_krig_annual_v2_0_0.txt (accessed 24 November 2020). GCOS Earth system energy observations are available from https://doi.org/10.26050/WDCC/GCOS_EHI_EXP. CMIP6 model data used in this paper is available from the Earth System Grid Federation at https://esgf-node.llnl.gov/search/cmip6/. Model data from the E3SM AMIP pre-industrial aerosol experiment is available from https://esgf-node.llnl.gov/projects/e3sm/.

References

Andrews, T., & Forster, P. M. (2020). Energy budget constraints on historical radiative forcing. *Nature Climate Change*, *10*(4), 313–316. https://doi.org/10.1038/s41558-020-0696-1

Andrews, T., Gregory, J. M., Paynter, D., Silvers, L. G., Zhou, C., Mauritsen, T., et al. (2018). Accounting for Changing Temperature Patterns Increases Historical Estimates of Climate Sensitivity. *Geophysical Research Letters*, *45*(16), 8490–8499. https://doi.org/10.1029/2018GL078887

Armour, K. C. (2017). Energy budget constraints on climate sensitivity in light of inconstant climate feedbacks. *Nature Climate Change*, *7*(5), 331–335. https://doi.org/10.1038/nclimate3278

Bellouin, N., Rae, J., Jones, A., Johnson, C., Haywood, J., & Boucher, O. (2011). Aerosol forcing in the Climate Model Intercomparison Project (CMIP5) simulations by HadGEM2-ES and the role of ammonium nitrate. *Journal of Geophysical Research Atmospheres*, *116*(20). https://doi.org/10.1029/2011JD016074

Bellouin, N., Quaas, J., Gryspeerdt, E., Kinne, S., Stier, P., Watson-Parris, D., et al. (2020). Bounding Global Aerosol Radiative Forcing of Climate Change. *Reviews of Geophysics*, *58*(1), e2019RG000660. https://doi.org/10.1029/2019RG000660

Bellouin, N., Davies, W., Shine, K. P., Quaas, J., Mülmenstädt, J., Forster, P. M., et al. (2020). Radiative forcing of climate change from the Copernicus reanalysis of atmospheric composition. *Earth System Science Data*, *12*(3), 1649–1677. https://doi.org/10.5194/essd-12-1649-2020

Bond, T. C., Doherty, S. J., Fahey, D. W., Forster, P. M., Berntsen, T., Deangelo, B. J., et al. (2013). Bounding the role of black carbon in the climate system: A scientific assessment. *Journal of Geophysical Research Atmospheres*, *118*(11), 5380–5552. https://doi.org/10.1002/jgrd.50171

Booth, B. B. B., Harris, G. R., Jones, A., Wilcox, L., Hawcroft, M., & Carslaw, K. S. (2018). Comments on "Rethinking the Lower Bound on Aerosol Radiative Forcing." *Journal of Climate*, *31*(22), 9407–9412. https://doi.org/10.1175/JCLI-D-17-0369.1

Boucher, O., Servonnat, J., Albright, A. L., Aumont, O., Balkanski, Y., Bastrikov, V., et al. (2020). Presentation and Evaluation of the IPSL-CM6A-LR Climate Model. *Journal of Advances in Modeling Earth Systems*, *12*(7). https://doi.org/10.1029/2019MS002010

Carslaw, K. S., Lee, L. A., Reddington, C. L., Pringle, K. J., Rap, A., Forster, P. M., et al. (2013). Large contribution of natural aerosols to uncertainty in indirect forcing. *Nature*, *503*(7474), 67–71. https://doi.org/10.1038/nature12674

Charlson, R. J., Schwartz, S. E., Hales, J. M., Cess, R. D., Coakley, J. A., Hansen, J. E., & Hofmann, D. J. (1992). Climate Forcing by Anthropogenic Aerosols. *Science*, *255*(5043), 423–430. https://doi.org/10.1126/science.255.5043.423

Collins, W. J., Lamarque, J.-F., Schulz, M., Boucher, O., Eyring, V., Hegglin, M. I., et al. (2017). AerChemMIP: quantifying the effects of chemistry and aerosols in CMIP6. *Geoscientific Model Development*, *10*(2), 585–607. https://doi.org/10.5194/gmd-10-585-2017

673 Cowtan, K., & Way, R. G. (2014). Coverage bias in the HadCRUT4 temperature series and its
674 impact on recent temperature trends. *Quarterly Journal of the Royal Meteorological*
675 *Society*, *140*(683), 1935–1944. https://doi.org/10.1002/qj.2297

676 Dunne, J. P., Horowitz, L. W., Adcroft, A. J., Ginoux, P., Held, I. M., John, J. G., et al. (2020).
677 The GFDL Earth System Model version 4.1 (GFDL-ESM 4.1): Overall coupled model
678 description and simulation characteristics. *Journal of Advances in Modeling Earth Systems*,
679 *Submitted*, 10.1029/2019MS002015. https://doi.org/10.1029/2019ms002015

680 Etminan, M., Myhre, G., Highwood, E. J., & Shine, K. P. (2016). Radiative forcing of carbon
681 dioxide, methane, and nitrous oxide: A significant revision of the methane radiative forcing.
682 *Geophysical Research Letters*, *43*(24), 12,614-12,623.
683 https://doi.org/10.1002/2016GL071930

684 Forest, C. E. (2018). Inferred Net Aerosol Forcing Based on Historical Climate Changes: a
685 Review. *Current Climate Change Reports*, *4*(1), 11–22. https://doi.org/10.1007/s40641-
686 018-0085-2

687 Forest, C. E., Stone, P. H., Sokolov, A. P., Allen, M. R., & Webster, M. D. (2002). Quantifying
688 uncertainties in climate system properties with the use of recent climate observations.
689 *Science*, *295*(5552), 113–117. https://doi.org/10.1126/science.1064419

690 Forest, C. E., Stone, P. H., & Sokolov, A. P. (2006). Estimated PDFs of climate system
691 properties including natural and anthropogenic forcings. *Geophysical Research Letters*,
692 *33*(1), n/a-n/a. https://doi.org/10.1029/2005GL023977

693 Geoffroy, O., Saint-Martin, D., Olivié, D. J. L., Voldoire, A., Bellon, G., & Tytéca, S. (2013).
694 Transient Climate Response in a Two-Layer Energy-Balance Model. Part I: Analytical
695 Solution and Parameter Calibration Using CMIP5 AOGCM Experiments. *Journal of*
696 *Climate*, *26*(6), 1841–1857. https://doi.org/10.1175/JCLI-D-12-00195.1

697 Geoffroy, O., Saint-Martin, D., Bellon, G., Voldoire, A., Olivié, D. J. L., & Tytéca, S. (2013).
698 Transient Climate Response in a Two-Layer Energy-Balance Model. Part II: Representation
699 of the Efficacy of Deep-Ocean Heat Uptake and Validation for CMIP5 AOGCMs. *Journal*
700 *of Climate*, *26*(6), 1859–1876. https://doi.org/10.1175/JCLI-D-12-00196.1

701 Ghan, S. J. (2013). Technical Note: Estimating aerosol effects on cloud radiative forcing.
702 *Atmospheric Chemistry and Physics*, *13*(19), 9971–9974. https://doi.org/10.5194/acp-13-
703 9971-2013

704 Ghan, S. J., Smith, S. J., Wang, M., Zhang, K., Pringle, K., Carslaw, K., et al. (2013). A simple
705 model of global aerosol indirect effects. *Journal of Geophysical Research: Atmospheres*,
706 *118*(12), 6688–6707. https://doi.org/10.1002/jgrd.50567

707 Ghimire, B., Williams, C. A., Masek, J., Gao, F., Wang, Z., Schaaf, C., & He, T. (2014). Global
708 albedo change and radiative cooling from anthropogenic land cover change, 1700 to 2005
709 based on MODIS, land use harmonization, radiative kernels, and reanalysis. *Geophysical*
710 *Research Letters*, *41*(24), 9087–9096. https://doi.org/10.1002/2014GL061671

711 Gidden, M. J., Riahi, K., Smith, S. J., Fujimori, S., Luderer, G., Kriegler, E., et al. (2019). Global
712 emissions pathways under different socioeconomic scenarios for use in CMIP6: a dataset of
713 harmonized emissions trajectories through the end of the century. *Geoscientific Model*
714 *Development*, *12*(4), 1443–1475. https://doi.org/10.5194/gmd-12-1443-2019

Global Volcanism Program. (2013). Volcanoes of the World v.4.9.0. Smithsonian Institution. https://doi.org/10.5479/si.GVP.VOTW4-2013

Golaz, J.-C., Caldwell, P. M., Van Roekel, L. P., Petersen, M. R., Tang, Q., Wolfe, J. D., et al. (2019). The DOE E3SM Coupled Model Version 1: Overview and Evaluation at Standard Resolution. *Journal of Advances in Modeling Earth Systems*, *11*(7), 2089–2129. https://doi.org/10.1029/2018MS001603

Gray, L. J., Rumbold, S. T., & Shine, K. P. (2009). Stratospheric Temperature and Radiative Forcing Response to 11-Year Solar Cycle Changes in Irradiance and Ozone. *Journal of the Atmospheric Sciences*, *66*(8), 2402–2417. https://doi.org/10.1175/2009JAS2866.1

Gregory, J. M., Andrews, T., Good, P., Mauritsen, T., & Forster, P. M. (2016). Small global-mean cooling due to volcanic radiative forcing. *Climate Dynamics*, *47*(12), 3979–3991. https://doi.org/10.1007/s00382-016-3055-1

Gregory, J. M., Andrews, T., Ceppi, P., Mauritsen, T., & Webb, M. J. (2020). How accurately can the climate sensitivity to CO 2 be estimated from historical climate change? *Climate Dynamics*, *54*(1–2), 129–157. https://doi.org/10.1007/s00382-019-04991-y

Hauglustaine, D. A., Balkanski, Y., & Schulz, M. (2014). A global model simulation of present and future nitrate aerosols and their direct radiative forcing of climate. *Atmospheric Chemistry and Physics*, *14*(20), 11031–11063. https://doi.org/10.5194/acp-14-11031-2014

Held, I. M., Winton, M., Takahashi, K., Delworth, T., Zeng, F., & Vallis, G. K. (2010). Probing the Fast and Slow Components of Global Warming by Returning Abruptly to Preindustrial Forcing. *Journal of Climate*, *23*(9), 2418–2427. https://doi.org/10.1175/2009JCLI3466.1

Held, I. M., Guo, H., Adcroft, A., Dunne, J. P., Horowitz, L. W., Krasting, J., et al. (2019). Structure and Performance of GFDL's CM4.0 Climate Model. *Journal of Advances in Modeling Earth Systems*, *11*(11), 3691–3727. https://doi.org/10.1029/2019MS001829

Hodnebrog, Ø., Myhre, G., Kramer, R. J., Shine, K. P., Andrews, T., Faluvegi, G., et al. (2020). The effect of rapid adjustments to halocarbons and N2O on radiative forcing. *Npj Climate and Atmospheric Science*, *3*(1). https://doi.org/10.1038/s41612-020-00150-x

Hodnebrog, Ø., Aamaas, B., Fuglestvedt, J. S., Marston, G., Myhre, G., Nielsen, C. J., et al. (2020). Updated Global Warming Potentials and Radiative Efficiencies of Halocarbons and Other Weak Atmospheric Absorbers. *Reviews of Geophysics*, *58*(3). https://doi.org/10.1029/2019RG000691

Hoesly, R. M., Smith, S. J., Feng, L., Klimont, Z., Janssens-Maenhout, G., Pitkanen, T., et al. (2018). Historical (1750–2014) anthropogenic emissions of reactive gases and aerosols from the Community Emissions Data System (CEDS). *Geoscientific Model Development*, *11*(1), 369–408. https://doi.org/10.5194/gmd-11-369-2018

Jiménez-de-la-Cuesta, D., & Mauritsen, T. (2019). Emergent constraints on Earth's transient and equilibrium response to doubled CO2 from post-1970s global warming. *Nature Geoscience*, *12*(11), 902–905. https://doi.org/10.1038/s41561-019-0463-y

Johnson, B. T., Haywood, J. M., & Hawcroft, M. K. (2019). Are Changes in Atmospheric Circulation Important for Black Carbon Aerosol Impacts on Clouds, Precipitation, and Radiation? *Journal of Geophysical Research: Atmospheres*, *124*(14), 7930–7950.

https://doi.org/10.1029/2019JD030568

Kelley, M., Schmidt, G. A., Nazarenko, L. S., Bauer, S. E., Ruedy, R., Russell, G. L., et al. (2020). GISS-E2.1: Configurations and Climatology. *Journal of Advances in Modeling Earth Systems*, *12*(8). https://doi.org/10.1029/2019MS002025

Knutti, R., Sedláček, J., Sanderson, B. M., Lorenz, R., Fischer, E. M., & Eyring, V. (2017). A climate model projection weighting scheme accounting for performance and interdependence. *Geophysical Research Letters*, *44*(4), 1909–1918. https://doi.org/10.1002/2016GL072012

Kovilakam, M., Thomason, L., Ernest, N., Rieger, L., Bourassa, A., & Millán, L. (2020). A Global Space-based Stratospheric Aerosol Climatology (Version 2.0): 1979--2018. *Earth System Science Data Discussions*, *2020*, 1–41. https://doi.org/10.5194/essd-2020-56

Kretzschmar, J., Salzmann, M., Mülmenstädt, J., Boucher, O., & Quaas, J. (2017). Comment on "Rethinking the Lower Bound on Aerosol Radiative Forcing." *Journal of Climate*, *30*(16), 6579–6584. https://doi.org/10.1175/JCLI-D-16-0668.1

Larson, E. J. L., & Portmann, R. W. (2016). A temporal kernel method to compute effective radiative forcing in CMIP5 transient simulations. *Journal of Climate*, *29*(4), 1497–1509. https://doi.org/10.1175/JCLI-D-15-0577.1

Lee, D. S., Fahey, D. W., Skowron, A., Allen, M. R., Burkhardt, U., Chen, Q., et al. (2020). The contribution of global aviation to anthropogenic climate forcing for 2000 to 2018. *Atmospheric Environment*, *244*, 117834. https://doi.org/10.1016/j.atmosenv.2020.117834

Lund, M. T., Myhre, G., Haslerud, A. S., Skeie, R. B., Griesfeller, J., Platt, S. M., et al. (2018). Concentrations and radiative forcing of anthropogenic aerosols from 1750 to 2014 simulated with the Oslo CTM3 and CEDS emission inventory. *Geoscientific Model Development*, *11*(12), 4909–4931. https://doi.org/10.5194/gmd-11-4909-2018

Lund, M. T., Myhre, G., & Samset, B. H. (2019). Anthropogenic aerosol forcing under the Shared Socioeconomic Pathways. *Atmospheric Chemistry and Physics*, *19*(22), 13827–13839. https://doi.org/10.5194/acp-19-13827-2019

Mahajan, S., Evans, K. J., Hack, J. J., & Truesdale, J. E. (2013). Linearity of Climate Response to Increases in Black Carbon Aerosols. *Journal of Climate*, *26*(20), 8223–8237. https://doi.org/10.1175/JCLI-D-12-00715.1

van Marle, M. J. E., Kloster, S., Magi, B. I., Marlon, J. R., Daniau, A.-L., Field, R. D., et al. (2017). Historic global biomass burning emissions for CMIP6 (BB4CMIP) based on merging satellite observations with proxies and fire models (1750–2015). *Geoscientific Model Development*, *10*(9), 3329–3357. https://doi.org/10.5194/gmd-10-3329-2017

Matthes, K., Funke, B., Andersson, M. E., Barnard, L., Beer, J., Charbonneau, P., et al. (2017). Solar forcing for CMIP6 (v3.2). *Geoscientific Model Development*, *10*(6), 2247–2302. https://doi.org/10.5194/gmd-10-2247-2017

Meinshausen, M., Meinshausen, N., Hare, W., Raper, S. C. B., Frieler, K., Knutti, R., et al. (2009). Greenhouse-gas emission targets for limiting global warming to 2°C. *Nature*, *458*(7242), 1158–1162. https://doi.org/10.1038/nature08017

Meinshausen, M., Vogel, E., Nauels, A., Lorbacher, K., Meinshausen, N., Etheridge, D. M., et al.

(2017). Historical greenhouse gas concentrations for climate modelling (CMIP6). *Geoscientific Model Development*, *10*(5), 2057–2116. https://doi.org/10.5194/gmd-10-2057-2017

Meinshausen, M., Nicholls, Z. R. J., Lewis, J., Gidden, M. J., Vogel, E., Freund, M., et al. (2020). The shared socio-economic pathway (SSP) greenhouse gas concentrations and their extensions to 2500. *Geoscientific Model Development*, *13*(8), 3571–3605. https://doi.org/10.5194/gmd-13-3571-2020

Murphy, D. M., Solomon, S., Portmann, R. W., Rosenlof, K. H., Forster, P. M., & Wong, T. (2009). An observationally based energy balance for the Earth since 1950. *Journal of Geophysical Research*, *114*(D17), D17107. https://doi.org/10.1029/2009JD012105

Myhre, G., Shindell, D., Bréon, F.-M., Collins, W., Fuglestvedt, J., Huang, J., et al. (2013). Anthropogenic and Natural Radiative Forcing. In Intergovernmental Panel on Climate Change (Ed.), *Climate Change 2013 - The Physical Science Basis* (pp. 659–740). Cambridge: Cambridge University Press. https://doi.org/10.1017/CBO9781107415324.018

Myhre, G., Samset, B. H., Schulz, M., Balkanski, Y., Bauer, S., Berntsen, T. K., et al. (2013). Radiative forcing of the direct aerosol effect from AeroCom Phase II simulations. *Atmospheric Chemistry and Physics*, *13*(4), 1853–1877. https://doi.org/10.5194/acp-13-1853-2013

Nicholls, Z. R. J., Meinshausen, M., Lewis, J., Gieseke, R., Dommenget, D., Dorheim, K., et al. (2020). Reduced complexity model intercomparison project phase 1: Protocol, results and initial observations. *Geoscientific Model Development Discussions*, *2020*, 1–33. https://doi.org/10.5194/gmd-2019-375

O'Rourke, P. R., Smith, S. J., McDuffie, E. E., Klimont, Z., Crippa, M., Mott, A., et al. (2020, September). CEDS v_2020_09_11 Pre-Release Emission Data. Zenodo. https://doi.org/10.5281/zenodo.4025316

Palmer, M. D. (2017). Reconciling Estimates of Ocean Heating and Earth's Radiation Budget. *Current Climate Change Reports*, *3*(1), 78–86. https://doi.org/10.1007/s40641-016-0053-7

Palmer, M. D., Harris, G. R., & Gregory, J. M. (2018). Extending CMIP5 projections of global mean temperature change and sea level rise due to thermal expansion using a physically-based emulator. *Environmental Research Letters*, *13*(8), 084003. https://doi.org/10.1088/1748-9326/aad2e4

Paulot, F., Paynter, D., Ginoux, P., Naik, V., & Horowitz, L. W. (2018). Changes in the aerosol direct radiative forcing from 2001 to 2015: observational constraints and regional mechanisms. *Atmospheric Chemistry and Physics*, *18*(17), 13265–13281. https://doi.org/10.5194/acp-18-13265-2018

Pincus, R., Forster, P. M., & Stevens, B. (2016). The Radiative Forcing Model Intercomparison Project (RFMIP): experimental protocol for CMIP6. *Geoscientific Model Development*, *9*(9), 3447–3460. https://doi.org/10.5194/gmd-9-3447-2016

Prather, M., Flato, G., Friedlingstein, P., Jones, C., Lamarque, J.-F., Liao, H., & Rasch, P. (2013). Climate System Scenario Tables. In Intergovernmental Panel on Climate Change (Ed.), *Climate Change 2013 - The Physical Science Basis* (pp. 1395–1446). Cambridge: Cambridge University Press. https://doi.org/10.1017/CBO9781107415324.030

Rap, A., Scott, C. E., Spracklen, D. V, Bellouin, N., Forster, P. M., Carslaw, K. S., et al. (2013). Natural aerosol direct and indirect radiative effects. *Geophysical Research Letters*, *40*(12), 3297–3301. https://doi.org/10.1002/grl.50441

Regayre, L. A., Pringle, K. J., Booth, B. B. B., Lee, L. A., Mann, G. W., Browse, J., et al. (2014). Uncertainty in the magnitude of aerosol-cloud radiative forcing over recent decades. *Geophysical Research Letters*, *41*(24), 9040–9049. https://doi.org/10.1002/2014GL062029

Richardson, M., Cowtan, K., Hawkins, E., & Stolpe, M. B. (2016). Reconciled climate response estimates from climate models and the energy budget of Earth. *Nature Climate Change*, *6*(10), 931–935. https://doi.org/10.1038/nclimate3066

Rogelj, J., Forster, P. M., Kriegler, E., Smith, C. J., & Séférian, R. (2019). Estimating and tracking the remaining carbon budget for stringent climate targets. *Nature*, *571*(7765), 335–342. https://doi.org/10.1038/s41586-019-1368-z

Rugenstein, M., Bloch-Johnson, J., Gregory, J., Andrews, T., Mauritsen, T., Li, C., et al. (2020). Equilibrium Climate Sensitivity Estimated by Equilibrating Climate Models. *Geophysical Research Letters*, *47*(4), e2019GL083898. https://doi.org/10.1029/2019GL083898

Von Schuckmann, K., Cheng, L., Palmer, M. D., Hansen, J., Tassone, C., Aich, V., et al. (2020). Heat stored in the Earth system: Where does the energy go? *Earth System Science Data*, *12*(3), 2013–2041. https://doi.org/10.5194/essd-12-2013-2020

Seland, Ø., Bentsen, M., Seland Graff, L., Olivié, D., Toniazzo, T., Gjermundsen, A., et al. (2020). The Norwegian Earth System Model, NorESM2 -- Evaluation of theCMIP6 DECK and historical simulations. *Geoscientific Model Development Discussions*, *2020*, 1–68. https://doi.org/10.5194/gmd-2019-378

Sellar, A. A., Jones, C. G., Mulcahy, J. P., Tang, Y., Yool, A., Wiltshire, A., et al. (2019). UKESM1: Description and Evaluation of the U.K. Earth System Model. *Journal of Advances in Modeling Earth Systems*, *11*(12), 4513–4558. https://doi.org/10.1029/2019MS001739

Sherwood, S., Dixit, V., & Salomez, C. (2018). The global warming potential of near-surface emitted water vapour. *Environmental Research Letters*, *13*(10). https://doi.org/10.1088/1748-9326/aae018

Sherwood, S., Webb, M. J., Annan, J. D., Armour, K. C., Forster, P. M., Hargreaves, J. C., et al. (2020). An assessment of Earth's climate sensitivity using multiple lines of evidence. *Reviews of Geophysics*, *n/a*(n/a), e2019RG000678. https://doi.org/10.1029/2019RG000678

Shindell, D., Lamarque, J.-F., Schulz, M., Flanner, M., Jiao, C., Chin, M., et al. (2013). Radiative forcing in the ACCMIP historical and future climate simulations. *Atmospheric Chemistry and Physics*, *13*(6), 2939–2974. https://doi.org/10.5194/acp-13-2939-2013

Skeie, R. B., Berntsen, T. K., Myhre, G., Tanaka, K., Kvalevåg, M. M., & Hoyle, C. R. (2011). Anthropogenic radiative forcing time series from pre-industrial times until 2010. *Atmospheric Chemistry and Physics*, *11*(22), 11827–11857. https://doi.org/10.5194/acp-11-11827-2011

Skeie, R. B., Berntsen, T., Aldrin, M., Holden, M., & Myhre, G. (2018). Climate sensitivity estimates – sensitivity to radiative forcing time series and observational data. *Earth System*

Dynamics, *9*(2), 879–894. https://doi.org/10.5194/esd-9-879-2018

Skeie, R. B., Myhre, G., Hodnebrog, Ø., Cameron-Smith, P. J., Deushi, M., Hegglin, M. I., et al. (2020). Historical total ozone radiative forcing derived from CMIP6 simulations. *Npj Climate and Atmospheric Science*, *3*(1). https://doi.org/10.1038/s41612-020-00131-0

Smith, C. J., Forster, P. M., Allen, M., Leach, N., Millar, R. J., Passerello, G. A., & Regayre, L. A. (2018). FAIR v1.3: a simple emissions-based impulse response and carbon cycle model. *Geoscientific Model Development*, *11*(6), 2273–2297. https://doi.org/10.5194/gmd-11-2273-2018

Smith, C. J., Kramer, R. J., Myhre, G., Forster, P. M., Soden, B. J., Andrews, T., et al. (2018). Understanding Rapid Adjustments to Diverse Forcing Agents. *Geophysical Research Letters*, *45*(21), 12,023-12,031. https://doi.org/10.1029/2018GL079826

Smith, C. J., Kramer, R. J., Myhre, G., Alterskjær, K., Collins, W., Sima, A., et al. (2020). Effective radiative forcing and adjustments in CMIP6 models. *Atmospheric Chemistry and Physics Discussions*, *2020*, 1–37. https://doi.org/10.5194/acp-2019-1212

Stevens, B. (2015). Rethinking the Lower Bound on Aerosol Radiative Forcing. *Journal of Climate*, *28*(12), 4794–4819. https://doi.org/10.1175/JCLI-D-14-00656.1

Stevenson, D. S., Young, P. J., Naik, V., Lamarque, J.-F., Shindell, D. T., Voulgarakis, A., et al. (2013). Tropospheric ozone changes, radiative forcing and attribution to emissions in the Atmospheric Chemistry and Climate Model Intercomparison Project (ACCMIP). *Atmospheric Chemistry and Physics*, *13*(6), 3063–3085. https://doi.org/10.5194/acp-13-3063-2013

Swart, N. C., Cole, J. N. S., Kharin, V. V, Lazare, M., Scinocca, J. F., Gillett, N. P., et al. (2019). The Canadian Earth System Model version 5 (CanESM5.0.3). *Geoscientific Model Development*, *12*(11), 4823–4873. https://doi.org/10.5194/gmd-12-4823-2019

Tanaka, K., & Raddatz, T. (2011). Correlation between climate sensitivity and aerosol forcing and its implication for the "climate trap." *Climatic Change*, *109*(3–4), 815–825. https://doi.org/10.1007/s10584-011-0323-2

Tatebe, H., Ogura, T., Nitta, T., Komuro, Y., Ogochi, K., Takemura, T., et al. (2019). Description and basic evaluation of simulated mean state, internal variability, and climate sensitivity in MIROC6. *Geoscientific Model Development*, *12*(7), 2727–2765. https://doi.org/10.5194/gmd-12-2727-2019

Taylor, K. E., Crucifix, M., Braconnot, P., Hewitt, C. D., Doutriaux, C., Broccoli, A. J., et al. (2007). Estimating Shortwave Radiative Forcing and Response in Climate Models. *Journal of Climate*, *20*(11), 2530–2543. https://doi.org/10.1175/JCLI4143.1

Thornhill, G. D., Collins, W. J., Kramer, R. J., Olivié, D., O'Connor, F., Abraham, N. L., et al. (2020). Effective Radiative forcing from emissions of reactive gases and aerosols -- a multimodel comparison. *Atmospheric Chemistry and Physics Discussions*, *2020*, 1–29. https://doi.org/10.5194/acp-2019-1205

Toohey, M., & Sigl, M. (2017). Volcanic stratospheric sulfur injections and aerosol optical depth from 500 BCE to 1900 CE. *Earth System Science Data*, *9*(2), 809–831. https://doi.org/10.5194/essd-9-809-2017

Vieira, L. E. A., Solanki, S. K., Krivova, N. A., & Usoskin, I. (2011). Evolution of the solar irradiance during the Holocene. *Astronomy & Astrophysics*, *531*, A6. https://doi.org/10.1051/0004-6361/201015843

Wilcox, L. J., Highwood, E. J., Booth, B. B. B., & Carslaw, K. S. (2015). Quantifying sources of inter-model diversity in the cloud albedo effect. *Geophysical Research Letters*, *42*(5), 1568–1575. https://doi.org/10.1002/2015GL063301

Williams, K. D., Copsey, D., Blockley, E. W., Bodas-Salcedo, A., Calvert, D., Comer, R., et al. (2018). The Met Office Global Coupled Model 3.0 and 3.1 (GC3.0 and GC3.1) Configurations. *Journal of Advances in Modeling Earth Systems*, *10*(2), 357–380. https://doi.org/10.1002/2017MS001115

Yukimoto, S., Kawai, H., Koshiro, T., Oshima, N., Yoshida, K., Urakawa, S., et al. (2019). The meteorological research institute Earth system model version 2.0, MRI-ESM2.0: Description and basic evaluation of the physical component. *Journal of the Meteorological Society of Japan*. https://doi.org/10.2151/jmsj.2019-051

Zelinka, M. D., Andrews, T., Forster, P. M., & Taylor, K. E. (2014). Quantifying components of aerosol-cloud-radiation interactions in climate models. *Journal of Geophysical Research: Atmospheres*, *119*(12), 7599–7615. https://doi.org/10.1002/2014JD021710